JOURNAL OF SPACECRAFT AND ROCKETS
Vol. 35, No. 5, September–October 1998

Numerical Simulation of a Supersonic Base-Bleed Projectile with Improved Turbulence Modeling

Petri Kaurinkoski* and Antti Hellsten†
Helsinki University of Technology, FIN-02015 HUT, Finland

Navier–Stokes simulations employing a k–ϵ turbulence model for the flow past a supersonic projectile with base bleed are discussed. A new method of avoiding turbulence-related problems near stagnation points is presented. The theoretical background of the modification is briefly described.

Nomenclature

c_f = local skin-friction coefficient, $\tau_w/(\rho_\infty V_\infty^2/2)$
c_p, c_v = specific heat at constant pressure and at constant density, J/(kg K)
D = shell diameter, m; Jacobian matrix of the source term Q, $(\partial Q/\partial U)$
d_w = thickness of the first cell on the surface, m
E = total internal energy per unit volume, J/m^3
e = specific internal energy, J/kg
$\boldsymbol{F}, \boldsymbol{G}, \boldsymbol{H}$ = flux vectors in the x, y, and z directions
H = total enthalpy per unit mass, J/kg
I = nondimensional base-bleed rate
$\boldsymbol{i}, \boldsymbol{j}, \boldsymbol{k}$ = unit vectors in Cartesian coordinate system
k = kinetic energy of turbulence, $\overline{u_{ii}''u_{ii}''}/2$, (m/s)^2
M = Mach number
$\dot{m}$ = mass flow rate through the inlet hole, kg/s
$\boldsymbol{n}$ = cell face unit normal vector
P = production of turbulent kinetic energy, J/m^{3}s
Pr = Prandtl number
p = static pressure, Pa
Re = Reynolds number, $\rho_\infty V_\infty D/\mu_\infty$
S, S_b = cell face area and area of the shell base, m^2
T = temperature, K
Tu = turbulence level, $\sqrt{(2k/3V^2)}$
$\boldsymbol{U}$ = vector of the conservative variables
V = cell volume, m^3; velocity $u\boldsymbol{i} + v\boldsymbol{j} + w\boldsymbol{k}$, m/s
y_n = normal distance from the surface, m
y^+ = nondimensional normal distance from the surface, $y_n\sqrt{(\rho_w\tau_w)}/\mu_w$
α = angle of attack
γ = ratio of specific heats c_p/c_v
δ = boundary-layer thickness, m
ϵ = dissipation of kinetic energy of turbulence, (m/s)^2/s
μ = dynamic viscosity, kg m/s
ρ = density, kg/m^3
σ = Schmidt number
τ = normal or shear stress, N/m^2
ϕ = mass fraction of a species; general scalar variable

Introduction

NOWADAYS trajectory simulations for artillery projectiles can be carried out quickly on any powerful personal computer or workstation. The reliability of these simulations depends on the accuracy of the atmospheric model and the accuracy of the aerodynamic model of the projectile. The trajectory simulations themselves are not too difficult and are performed routinely.

During the past few decades, computational techniques for the simulation of different types of jets for controlling the flight of projectiles[1–3] have been developed. With projectiles, the practical aim is to extend the firing range, i.e., to reduce the base drag by bleeding gas from the base of the shell. As a part of the design process, numerical simulations are widely used for analyzing the different design options. There are, however, many unanswered questions regarding the reliability of the numerical simulations: Turbulence modeling always incorporates some uncertainty, and the thermodynamic as well as chemical properties of the bled gas are probable sources of errors. To become a valuable design tool, computational fluid dynamics (CFD) has to show reliability and robustness. Otherwise, only limited types of cases can be simulated, and the whole potential of CFD is not utilized.

We present results of Navier–Stokes simulations for a supersonic projectile with base bleed. The freestream Mach number is fixed to 1.2, and the angle of attack is 5 deg. The same projectile was studied at zero angle of attack by Kaurinkoski[4] in varying flow conditions. In this work, a slight modification to the widely used low Reynolds number k–ϵ model of Chien[5] is proposed to avoid unphysical anomalies near the stagnation point.

The Navier–Stokes solver used for the simulations is FINFLO. The code has been developed at the Helsinki University of Technology in the Laboratory of Aerodynamics. It is based on the finite volume method and is capable of handling three-dimensional multiblock grids. The solution method is implicit pseudotime integration with a multigrid acceleration of convergence. In the simulations, Roe's flux-difference splitting is applied for the inviscid fluxes, and central differences are used for the friction terms. The FINFLO code is described in more detail in Ref. 6. In this work, the effects of turbulence are taken into account using Chien's low-Reynolds-number k–ϵ model with a slight modification.

The two-equation turbulence models employing Boussinesq's approximation are known to overpredict the production of turbulent kinetic energy near stagnation points. This may lead to dramatically overestimated turbulence levels near the stagnation point, which in turn may spoil the whole solution farther downstream. To avoid problems related to this excessive production, Menter[7] suggested an upper limit based on experimental results. A modification to that limit is suggested in this paper. The current modification is an extension to the upper limit for the production of turbulent kinetic energy. The idea is to utilize a stronger limit outside shear layers and the original limit inside shear layers. The local level of vorticity is employed for determining whether we reside in a shear layer or not.

In comparison with results obtained employing the standard version of Chien's k–ϵ model, the current results are superior in quality near the stagnation region. The base area, however, remains an area of uncertainty. The proposed limit for turbulence production increases the robustness of the solver inasmuch as development of turbulence is slightly damped.

Received Sept. 8, 1997; revision received May 16, 1998; accepted for publication June 1, 1998.

*Research Scientist, Laboratory of Aerodynamics, P.O. Box 4400. E-mail: Petri.Kaurinkoski@hut.fi. Member AIAA.
†Research Scientist, Laboratory of Aerodynamics, P.O. Box 4400. E-mail: Antti.Hellsten@hut.fi. Member AIAA.

Numerical Method

Governing Equations in Differential Form

The Reynolds-averaged Navier–Stokes equations, the equations for the kinetic energy k and dissipation ϵ of turbulence, and the scalar transport equation can be written in the following differential form:

$$\frac{\partial \boldsymbol{U}}{\partial t} + \frac{\partial(\boldsymbol{F}-\boldsymbol{F}_v)}{\partial x} + \frac{\partial(\boldsymbol{G}-\boldsymbol{G}_v)}{\partial y} + \frac{\partial(\boldsymbol{H}-\boldsymbol{H}_v)}{\partial z} = Q \tag{1}$$

where $\boldsymbol{U} = (\rho, \rho u, \rho v, \rho w, E, \rho k, \rho\epsilon, \rho\phi)^T$. The inviscid fluxes in the x, y, and z directions are denoted by $\boldsymbol{F}$, $\boldsymbol{G}$, and $\boldsymbol{H}$, respectively. For example, $\boldsymbol{F}$ is given by

$$\boldsymbol{F} = \begin{bmatrix} \rho u \\ \rho u^2 + p + \frac{2}{3}\rho k \\ \rho v u \\ \rho w u \\ \left(E + p + \frac{2}{3}\rho k\right)u \\ \rho u k \\ \rho u \epsilon \\ \rho u \phi \end{bmatrix} \tag{2}$$

where $\rho\phi$ is the density of the bled gas. The total internal energy E is defined as

$$E = \rho e + \rho\frac{u^2+v^2+w^2}{2} + \rho k \tag{3}$$

In a similar manner, the viscous fluxes in the x, y, and z directions are $\boldsymbol{F}_v$, $\boldsymbol{G}_v$, and $\boldsymbol{H}_v$, respectively. For example, $\boldsymbol{F}_v$ is given by

$$\boldsymbol{F}_v = \begin{bmatrix} 0 \\ \tau_{xx} + \frac{2}{3}\rho k \\ \tau_{xy} \\ \tau_{xz} \\ u\left(\tau_{xx} + \frac{2}{3}\rho k\right) + v\tau_{xy} + w\tau_{xz} - q_x \\ \mu_k\left(\dfrac{\partial k}{\partial x}\right) \\ \mu_\epsilon\left(\dfrac{\partial \epsilon}{\partial x}\right) \\ \mu_\phi\left(\dfrac{\partial \phi}{\partial x}\right) \end{bmatrix} \tag{4}$$

where the viscous stress tensor is

$$\tau_{ij} = \mu\left[\frac{\partial u_j}{\partial x_i} + \frac{\partial u_i}{\partial x_j} - \frac{2}{3}(\nabla\cdot\boldsymbol{V})\delta_{ij}\right] - \overline{\rho u_i'' u_j''} \tag{5}$$

For the Reynolds stresses, we use Boussinesq's approximation

$$-\overline{\rho u_i'' u_j''} = \mu_T\left[\frac{\partial u_j}{\partial x_i} + \frac{\partial u_i}{\partial x_j} - \frac{2}{3}(\nabla\cdot\boldsymbol{V})\delta_{ij}\right] - \frac{2}{3}\rho k\delta_{ij} \tag{6}$$

where μ_T is a turbulent viscosity coefficient. In the momentum and energy equations, the kinetic energy contribution has been connected with pressure and appears in the convective fluxes. The viscous terms contain a laminar and a turbulent part. Similarly, the heat flux is written as

$$\boldsymbol{q} = -[\mu(c_p/Pr) + \mu_T(c_p/Pr_T)]\nabla T + \boldsymbol{q}_D \tag{7}$$

where $\boldsymbol{q}_D$ is the energy flux due to diffusion of mass.[8] The pressure is calculated from an equation of state $p = p(\rho, e)$, which, for a calorically perfect gas, is written

$$p = (\gamma-1)\left(E - \rho\frac{u^2+v^2+w^2}{2} - \rho k\right) = (\gamma-1)\rho e \tag{8}$$

The diffusion coefficients of the turbulence quantities and the scalar quantity are approximated as

$$\mu_k = \mu + (\mu_T/\sigma_k), \qquad \mu_\epsilon = \mu + (\mu_T/\sigma_\epsilon)$$
$$\mu_\phi = \left(\mu/\sigma_{\phi_L}\right) + \left(\mu_T/\sigma_{\phi_T}\right) \tag{9}$$

where σ_k, σ_ϵ, and σ_ϕ are the appropriate Schmidt numbers and μ_T is the turbulent viscosity of the fluid determined with any turbulence model. The source term Q has nonzero components for the equations for turbulence and possibly for the scalar equation.

Turbulence Modeling

The solution is extended to the wall instead of using a wall-function approach. Near the wall, the low-Reynolds-number model proposed by Chien[5] is adopted. The source terms for k and ϵ in Chien's model are given as

$$Q = \begin{bmatrix} P - \rho\epsilon - 2\mu\left(k/y_n^2\right) \\ c_1(\epsilon/k)P - c_2(\rho\epsilon^2/k) - 2\mu\left(\epsilon/y_n^2\right)e^{-y^+/2} \end{bmatrix} \tag{10}$$

where y^+ is defined by

$$y^+ = y_n\frac{\rho u_\tau}{\mu} = y_n\frac{\sqrt{\rho\tau_w}}{\mu} = y_n\left[\frac{\rho|\nabla\times\boldsymbol{V}|}{\mu}\right]_w^{\frac{1}{2}} \tag{11}$$

The production of turbulent kinetic energy is modeled using Eq. (6) as

$$P = -\overline{\rho u_i'' u_j''}\frac{\partial u_i}{\partial x_j}$$
$$= \left[\mu_T\left(\frac{\partial u_i}{\partial x_j} + \frac{\partial u_j}{\partial x_i} - \frac{2}{3}\delta_{ij}\frac{\partial u_k}{\partial x_k}\right) - \frac{2}{3}\delta_{ij}\rho k\right]\frac{\partial u_i}{\partial x_j} \tag{12}$$

In the k–ϵ model, the turbulent viscosity is calculated from

$$\mu_T = c_\mu(\rho k^2/\epsilon) \tag{13}$$

The equations for k and ϵ contain empirical coefficients. These are given by

$$c_1 = 1.44, \qquad \sigma_k = 1.0$$
$$c_2 = 1.92\left(1 - 0.22e^{-Re_T^2/36}\right), \qquad \sigma_\epsilon = 1.3 \tag{14}$$
$$c_\mu = 0.09\left(1 - e^{-0.0115y^+}\right)$$

where the turbulence Reynolds number is defined as

$$Re_T = \rho k^2/\mu\epsilon \tag{15}$$

Chien proposed slightly different forms for c_1 and c_2. Because the computations performed for the flat-plate boundary layer[9] appeared to be insensitive to the modifications, formulas (14) were based on the most commonly used coefficients $c_1 = 1.44$ and $c_2 = 1.92$.

Treatment of the Production of Turbulence

A common problem with turbulence models employing Boussinesq's approximation is the inability to accurately account for streamline curvature effects. Therefore, production of turbulent kinetic energy is easily overpredicted with Eq. (12) in regions of curved flow.

To avoid unphysical growth of the turbulent viscosity μ_T, e.g., near stagnation points, Menter[7] suggested a limit for the production of turbulent kinetic energy P as

$$P = \min(P, 20\,\rho\epsilon) \tag{16}$$

According to the tests conducted,[7] the maximum of the ratio $P/\rho\epsilon$ inside shear layers is about two and, therefore, this limit should not affect the well-behaving regions of the flowfield. Only the problems

encountered near the stagnation point should disappear. In addition, this limiter has some effect on the solution of shock waves.

We have previously employed Eq. (16) successfully, but in the present simulation this limit was not strong enough. The turbulence production was overpredicted in front of the stagnation point, and as a consequence the whole solution near the stagnation point was spoiled. Quite evidently, unphysical turbulence production was also predicted for the inviscid flowfield outside the boundary layer on the nose.

To differentiate between shear-layer regions and inviscid regions, we monitor the level of vorticity. A crude estimate for the level of vorticity encountered inside shear layers is based on laminar boundary-layer flow solution. The boundary-layer thickness is given by

$$\delta = \frac{5.3\, L_{\text{ref}}}{\sqrt{Re_\infty}} \tag{17}$$

and an estimate for the level of vorticity inside the boundary layer is

$$\Omega_{\text{ref}} \approx C_\Omega \frac{V_\infty}{\delta} = C_\Omega \frac{V_\infty \sqrt{Re_\infty}}{5.3\, L_{\text{ref}}} \tag{18}$$

where $Re_\infty = \rho_\infty V_\infty L_{\text{ref}}/\mu_\infty$ and C_Ω is a model parameter set to 0.03 in the present simulations. Outside shear layers, the limit for production would be $2\rho\epsilon$, whereas inside shear layers, the original value of $20\rho\epsilon$ is utilized. For a smooth transition between the two regions a hyperbolic tangent function is employed as

$$P_{\max} = \left\{ 2 + 18 \tanh\left[\left(\frac{|\nabla \times V|}{\Omega_{\text{ref}}} \right)^{n_\omega} \right] \right\} \rho\epsilon \tag{19}$$

Here the exponent $n_\omega = 4$ is also a selected model parameter. Later we will refer to Eq. (19) as the vorticity-based production limit (VBPL).

The selected model parameters were tested with a basic flat-plate flow, with a few two-dimensional simulations with airfoils, and with the present projectile simulations. The other solutions remained unchanged, whereas the projectile simulation was favorably changed. For different types of flows, the model parameters may need some fine tuning.

This limit may have an effect on the location of the transition point, but in the performed two-dimensional tests, no change was observed. It is, therefore, our belief that the final steady-state solution, in cases where turbulence production does not cause problems, is not changed, but the iteration time history is altered.

Finite Volume Form and Discretization of the Inviscid Fluxes

A finite volume technique is applied. The flow equations have an integral form

$$\frac{\mathrm{d}}{\mathrm{d}t} \int_V \boldsymbol{U}\, \mathrm{d}V + \int_S \boldsymbol{F}(\boldsymbol{U}) \cdot \mathrm{d}\boldsymbol{S} = \int_V Q\, \mathrm{d}V \tag{20}$$

for an arbitrary fixed region V with a boundary S. Performing the integrations for a computational cell i yields

$$V_i \frac{\mathrm{d}U_i}{\mathrm{d}t} = \sum_{\text{faces}} - S\hat{\boldsymbol{F}} + V_i Q_i \tag{21}$$

where S is the area of the cell face and the sum is taken over the faces of the computational cell. The inviscid parts of the fluxes are evaluated with Roe's method.[10] The flux is calculated as

$$\hat{\boldsymbol{F}} = T^{-1} \boldsymbol{F}(T\boldsymbol{U}) \tag{22}$$

where T is a rotation matrix, which transforms the dependent variables to a local coordinate system normal to the cell surface. In this way, only the Cartesian form $\boldsymbol{F}$ of the flux is needed.

Calculation of the Viscous Fluxes and the Source Term

The viscous fluxes are evaluated using a central difference approximation, which is applied in all of the curvilinear coordinate directions. For the derivatives in the production term of turbulent kinetic energy (12), however, the thin-layer model is not applied. Instead, the derivatives are calculated exactly.

The possible wall corrections of the turbulent viscosity, as well as those of the source terms, are calculated separately in the i, j, and k directions. As a result, the source term may contain several wall correction terms, and the wall damping of turbulent viscosity is a product of the different wall-damping terms in different coordinate directions if several walls are present.

Boundary Conditions

At the freestream boundary, the values of the dependent variables are kept as constants. However, in regions where the freestream velocity is directed out from the computational domain, the boundary values are extrapolated. In the flowfield, k and ϵ are limited from below to their freestream values. In the calculation of the inviscid fluxes at the solid boundary, the flux-difference splitting is not used. Because the convective speed is equal to zero on the solid surfaces, the only contribution to the inviscid surface fluxes arises from the pressure terms in the momentum equations. A second-order extrapolation is applied for the evaluation of the wall pressure as

$$p_w = \tfrac{3}{2} p_1 - \tfrac{1}{2} p_2 \tag{23}$$

where the subscript w refers to conditions on the wall and 1 and 2 refer to the center of the first and second cell from the surface, respectively. A similar formula is used for the diffusion coefficients on the wall.

The viscous fluxes on the solid surfaces are obtained by setting $u = v = w = 0$ on the wall. The central expression of the viscous terms is replaced by a second-order, one-sided formula,

$$\frac{\partial \phi}{\partial y_n} = \frac{-8\phi_w + 9\phi_1 - \phi_2}{3 d_w} \tag{24}$$

The boundary condition for the energy equation can be determined in two ways: Either the wall temperature is set to a predefined temperature or the wall is assumed to be adiabatic. The latter method is employed. The viscous fluxes of k and ϵ, as well as ϕ_i, are also set to zero at the wall. In this way there is no need to specify the surface values of the turbulence quantities.

Specification of the Inlet Boundary Conditions

The base-bleed boundary is an inlet-type boundary condition because there is flow into the computational domain. However, the boundary condition has to be carefully set, based on the given constraints and the local flowfield conditions.

We specify the mass flow rate $\dot{m}$, total enthalpy H, and static pressure of the inlet. In addition, the turbulence level Tu and the turbulent viscosity μ_T are specified for the k–ϵ model. The turbulent viscosity is needed only for the specification of the dissipation of turbulent kinetic energy $\rho\epsilon$ at the inlet. In the present case, the local velocity is used as the reference velocity for turbulence level. Naturally, the mass fractions of the species are also specified.

For a subsonic inlet, the static pressure p is extrapolated from the flowfield, whereas in a supersonic inlet, all of the conditions should be set from the inlet side. In practice, the inlet pressure is limited from below with a sonic pressure based on the given $\dot{m}$ and H. For more details, see Ref. 11.

Solution Algorithm

The discretized equations are integrated in pseudotime applying the diagonally dominant alternating direction implicit factorization.[12] This is based on the approximate factorization and on the splitting of the Jacobians of the flux terms. The resulting implicit stage consists of a backward and forward sweep in every coordinate direction, as described in Ref. 9. The sweeps are based on a first-order upwind differencing. In addition, the linearization of the source term is factored out of the spatial sweeps. The boundary conditions are treated explicitly, and a spatially varying time step is utilized.

To simplify the linearization of the source term Q, the wall-reflection terms involving wall distances are not linearized. Also,

for stability reasons, only negative source terms are linearized in the Jacobian matrix D. To account for the positive source terms Q^+, the following trick is applied:

$$\frac{\partial Q^+}{\partial \boldsymbol{U}} = -\frac{Q}{|\Delta \boldsymbol{U}_{\max}|} \tag{25}$$

In this way, the maximum change of $\boldsymbol{U}$ caused by Q is limited to $|\Delta \boldsymbol{U}_{\max}|$. The actual limit may be evaluated in many ways. Currently, the contributions of P are included in a very approximate fashion: The maximum change of ρk is limited with $\min(|0.1E - \rho k|, \rho k)$. For the production term in the ϵ equation, the maximum change of $\rho\epsilon$ is set to $(\rho\epsilon/\rho k)\Delta(\rho k)_{\max}$. A further simplification is to utilize the trick suggested by Vandromme[13]:

$$-\rho\epsilon = -c_\mu \frac{(\rho k)^2}{\mu_T} \tag{26}$$

Another simplification is to ignore the off-diagonal terms in D, and the final form of D becomes

$$\frac{\partial Q}{\partial \boldsymbol{U}} = \begin{bmatrix} -\dfrac{|P|}{|\Delta(\rho k)_{\max}|} - 2\dfrac{\rho\epsilon}{\rho k} & 0 \\ 0 & -c_1 \dfrac{(\rho\epsilon/\rho k)|P|}{|\Delta(\rho\epsilon)_{\max}|} - 2c_2 \dfrac{\rho\epsilon}{\rho k} \end{bmatrix} \tag{27}$$

To accelerate convergence, a multigrid method is employed. The multigrid cycling employs a V cycle and is based on the method by Jameson and Yoon.[14] The details of the implementation are found in Ref. 15.

Modeling of the High-Temperature Effects and the Mixture Properties

The thermodynamic properties of a mixture of gases can be determined by analyzing the thermodynamics of the components of the mixture. Each component in turn is a thermally perfect gas, and the difficulty of the whole problem is divided into smaller ones. We have chosen to employ existing algebraic interpolation equations for the specific heats of all of the components in the mixture, and consequently the mixture model has the same functional form. With the model for specific heats, the equation of state is closed, and the remaining problem is to solve for T with a given e and ρ. The details are shown in Ref. 4.

The transport properties of a mixture are determined employing Sutherland's formula for viscosity for each species, and the mixture properties are obtained with Wilke's rule.[16] The same procedure is applied for thermal conductivity.

Computational Grids

All of the presented results are for a 155-mm-diam supersonic dome-based long-range projectile. A four-block axially symmetric grid with $144 \times 64 \times 12$ cells in the axial, near-normal, and circumferential directions, respectively, in each block is employed for modeling the geometry of the projectile. The block division was necessary only for parallelization purposes.

In total there are 48 cells in the radial direction on the base surface. The inlet hole was modeled with an 8×12 patch in each block on the base surface. The y^+ value in the center of the first cell above the surface was kept below 1. The grid around the projectile is seen in Fig. 1. The diameter of the base-bleed hole is 0.0476 m.

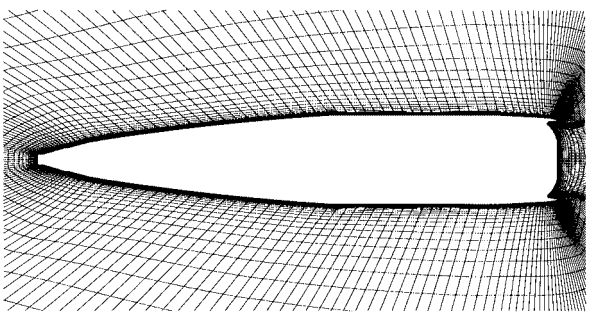

Fig. 1 Grid around the dome-based artillery shell.

Computed Test Case

One flow case is studied where $M_\infty = 1.2$, $Re_\infty = 1.4 \times 10^6$, and $\alpha = 5$ deg. The mass flow rate is $\dot{m} = 0.018$ kg/s, which is usually expressed with the nondimensional quantity $I = 0.009$ defined by

$$I = \frac{\dot{m}}{\rho_\infty V_\infty S_b} \tag{28}$$

The total temperature of the bled gas was set to 2370 K. The specified turbulence level Tu and the ratio of turbulent and laminar viscosity μ_T/μ at the jet inlet were constants, 5% and 50, respectively. The freestream air is treated as a calorically perfect gas, and the composition and the model parameters for the bled gas are the same as those employed in Ref. 4.

Computational Results

A standard procedure in our simulations is to calculate an initial estimate for the simulations on a coarser grid employing the multigrid routines. Therefore, simulations are usually initiated from the third grid level with the number of cells reduced to $\frac{1}{64}$ of the finest grid. Results from level 3 are used as an initial condition for level 2, and likewise the solution on level 2 is an initial state for level 1. In this way, the number of iteration cycles required on the finest grid level is reduced by 20–50%, and sometimes a fatal initial transient can be avoided by the coarse-grid initialization. We should also note that, for stability reasons and to maintain comparability, the multigrid scheme was not employed to accelerate convergence in any of these computations.

The iteration histories showed some interesting properties. Without VBPL, the problems at the nose of the body were present on all grid levels. The convergence properties showed no clear indications of the problems encountered near the stagnation point, but a closer look at the solution revealed some anomalies from both the turbulence-related quantities and the basic flow variables. A very strange slice of increased density and reduced temperature appeared on the surface of the nose, and the ρk as well as μ_T distributions also had strange peaks in the same area.

If the fine-grid simulations were started from an initial estimate obtained by employing VBPL, the solution remained free of these problems, and a steady solution was reached in 8000 cycles. Therefore, it seems the problem is actually only a matter of transient abnormal behavior of the flow solution. To investigate this, computation without VBPL on the second grid level was continued from the essentially converged steady solution. After another 3000 iteration cycles, the anomalies had vanished almost completely. With VBPL, however, the problems never appeared at all.

Another test was to completely omit the coarse-grid simulations and start the simulations on the finest grid level with initially freestream flow. Regardless of the treatment of turbulence production, however, the iteration would fail because of numerical problems behind the base.

It is not completely certain whether production of turbulence is the true origin of these problems, but at least one solution is to employ Eq. (19), i.e., VBPL. Some properties of the solution indicate that the problems were partially related to the properties of the grid.

To isolate the effects of VBPL, we computed the case with and without VBPL starting from the same coarse-grid initial estimate generated without VBPL. Figure 2a shows the distribution of P and $\rho\epsilon$ as a function of the distance to the wall along a grid line pointing upstream in the symmetry plane (block $= 4$, $i = 5$, $k = 13$) after 100 iteration cycles on the finest grid level. Note that the indices given here refer to grid corner points and not cell center points. Without VBPL, the solution has a strong second peak for P at $y \approx 4.1$ mm, which is filtered out with the modified limiter. The $\rho\epsilon$ distribution in Fig. 2a shows slight changes by the VBPL. The main thing here is that without VBPL there is a huge imbalance between P and $\rho\epsilon$ and thus locally much more ρk is generated than dissipated. For steady state, this would require an equal and opposite imbalance for the fluxes (convection and diffusion). There is no reason for such an imbalance of fluxes on the freestream side of the stagnation point.

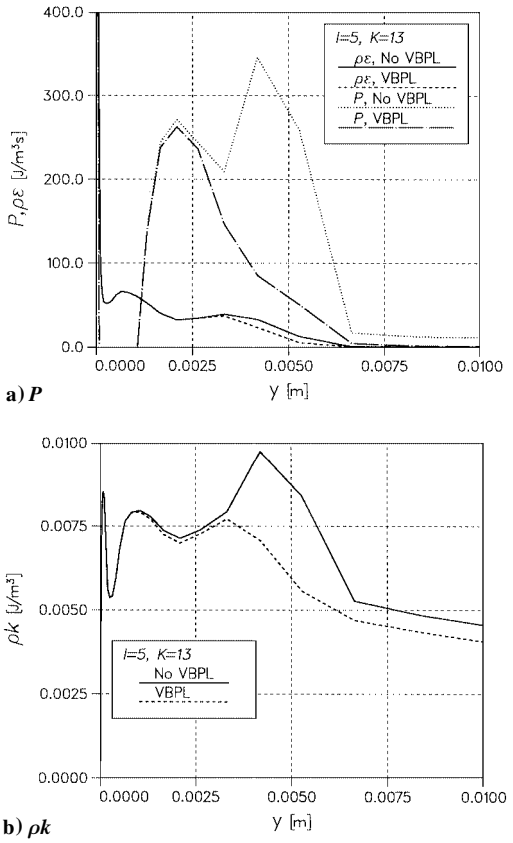

Fig. 2 Distributions in the symmetry plane upstream of the stagnation point after 100 iteration cycles, where *y* is distance to the wall.

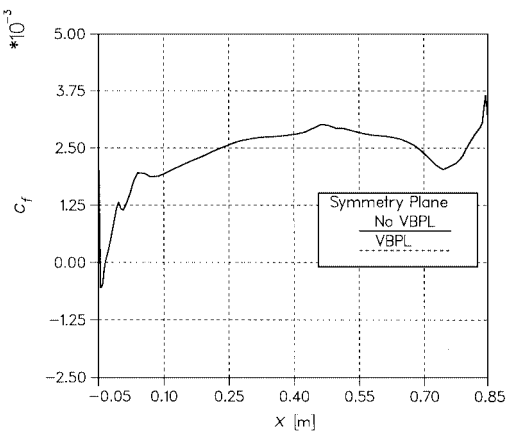

Fig. 3 Skin-friction coefficient c_f distributions after 2000 iteration cycles.

Figure 2b shows what has happened to ρk after 100 iteration cycles. Clearly, the distribution with VBPL is smoother and in that sense seems more reasonable. After all, there should not be too much upstream influence from the stagnation region.

The uncertainty about using VBPL is in what happens to the basic flow solution. To demonstrate that the basic features are not changed at all, Fig. 3 shows the c_f distribution on the upper surface of the shell in the symmetry plane after 2000 iteration cycles. The curves corresponding to VBPL and no VBPL are indistinguishable, which confirms that no dramatic changes in the basic solution have arisen.

Continuing the simulations to 2000 cycles smoothed out the worst peaks in P and ρk, but it is interesting to see in Fig. 4a how $\rho\epsilon$ is not affected at all, whereas the ρk level (Fig. 4b) without VBPL is approximately 15% higher than with VBPL. Nonetheless, the P distributions are now quantitatively similar.

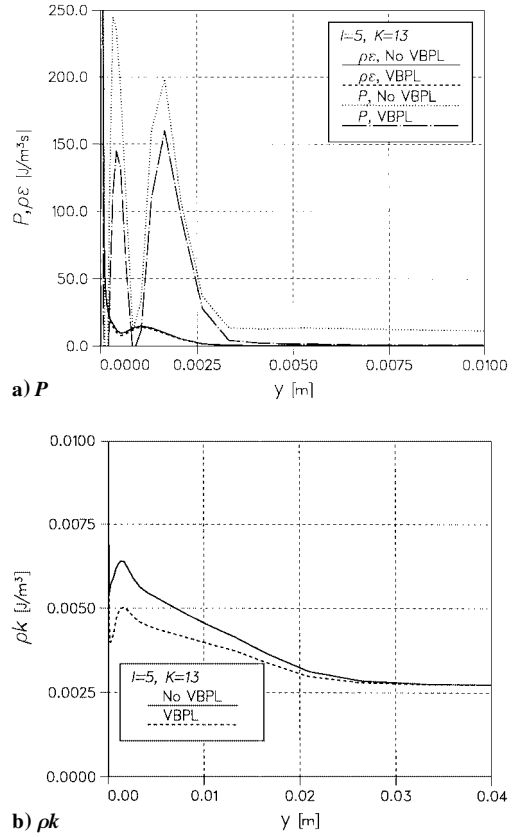

Fig. 4 Distributions in the symmetry plane upstream of the stagnation point after 2000 iteration cycles, where *y* is distance to the wall.

Conclusions

We have numerically solved the supersonic flow past a base-bleed projectile. We have developed a hybrid upper limit for the production of turbulent kinetic energy to avoid problems related to stagnation point regions.

The results show that production of turbulent kinetic energy is changed, and consequently, the level of ρk is lower than without the VBPL. The final solution is not changed too much, but transient peaks in ρk and P distributions are avoided.

If used with care, the VBPL can solve some of the problems in estimating P with the Boussinesq's approximations. However, in areas where excessive production of turbulence is not a problem, the solution remains unchanged.

Acknowledgment

This research project has been funded by MATINE, the Scientific Committee of National Defence, Helsinki, Finland. Its support for this research is gratefully acknowledged.

References

[1] Sahu, J., and Heavey, K. R., "Numerical Investigation of Supersonic Base Flow with Base Bleed," *Journal of Spacecraft and Rockets*, Vol. 34, No. 1, 1997, pp. 62–69.

[2] Nusca, M. J., "Numerical Simulation of Gas Dynamics and Combustion for 120-mm Ram Accelerator," *Proceedings of the 14th International Symposium on Ballistics*, edited by M. J. Murphy, and J. E. Backofen, Vol. 1, American Defence Preparedness Association, Arlington, VA, 1993, pp. 261–272.

[3] Sahu, J., Nietubicz, C. J., and Steger, J. L., "Navier–Stokes Computations of Projectile Base Flow With and Without Mass Injection," *AIAA Journal*, Vol. 23, No. 9, 1985, pp. 1348–1355.

[4] Kaurinkoski, P., "Computation of the Flow of Thermally Perfect Gas Past a Supersonic Projectile with Base Bleed," *Proceedings of the AIAA Atmospheric Flight Mechanics Conference*, AIAA, Reston, VA, 1996, pp. 725–734 (AIAA Paper 96-3451).

[5] Chien, K.-Y., "Predictions of Channel and Boundary-Layer Flows with a Low-Reynolds-Number Turbulence Model," *AIAA Journal*, Vol. 20, No. 1, 1982, pp. 33–38.

[6]Kaurinkoski, P., Salminen, E., and Siikonen, T., "Computation of Turbulent Flow over Finned Projectiles," *Proceedings of the AIAA Atmospheric Flight Mechanics Conference*, AIAA, Washington, DC, 1994, pp. 378–387 (AIAA Paper 94-3502).

[7]Menter, F. R., "Zonal Two Equation k–ω Turbulence Models for Aerodynamic Flows," AIAA Paper 93-2906, July 1993.

[8]Anderson, J. D., Jr., *Hypersonic and High Temperature Gas Dynamics*, McGraw–Hill, New York, 1989, pp. 600–602.

[9]Siikonen, T., "An Application of Roe's Flux-Difference Splitting for the k–ϵ Turbulence Model," *International Journal for Numerical Methods in Fluids*, Vol. 21, 1995, pp. 1017–1039.

[10]Roe, P., "Approximate Riemann Solvers, Parameter Vectors, and Difference Schemes," *Journal of Computational Physics*, Vol. 43, 1981, pp. 357–372.

[11]Kaurinkoski, P., "Numerical Determination of the Flow of an Arbitrary Mixture of Gases," Licentiate Thesis, Dept. of Mechanical Engineering, Helsinki Univ. of Technology, Finland, Dec. 1995.

[12]Lombard, C., Bardina, J., Venkatapathy, E., and Oliger, J., "Multi-Dimensional Formulation of CSCM—An Upwind Flux Difference Eigenvector Split Method for the Compressible Navier–Stokes Equations," *Proceedings of the AIAA 6th Computational Fluid Dynamics Conference*, AIAA, New York, 1983, pp. 649–664 (AIAA Paper 83-1895).

[13]Vandromme, D., "Turbulence Modeling for Turbulent Flows and Implementation in Navier–Stokes Solvers," *Introduction to the Modeling of Turbulence*, edited by C. Benocci, Lecture Series 1991-02, von Kármán Inst. for Fluid Dynamics, 1991.

[14]Jameson, A., and Yoon, S., "Multigrid Solution of the Euler Equations Using Implicit Schemes," *AIAA Journal*, Vol. 24, No. 11, 1986, pp. 1737–1743.

[15]Siikonen, T., Hoffren, J., and Laine, S., "A Multigrid LU Factorization Scheme for the Thin-Layer Navier–Stokes Equations," *Proceedings of the 17th ICAS Congress* (Stockholm, Sweden), International Council of the Aeronautical Sciences, 1990, pp. 2023–2034 (ICAS Paper 90-6.10.3).

[16]White, F. M., *Viscous Fluid Flow*, 2nd ed. McGraw–Hill, New York, 1991, pp. 34, 35.

R. M. Cummings
Associate Editor